A comprehensive study of binder polymer for supercapattery electrode based on activated carbon and nickel-silicon composite

by Munasir Munasir

Submission date: 29-Mar-2023 05:20AM (UTC+0700)
Submission ID: 2049411100
File name: Materials_Science_for_Energy_Technologies_6_2023_368_381.pdf (6.27M)
Word count: 12163
Character count: 64016

Materials Science for Energy Technologies 6 (2023) 368–381

Contents lists available at ScienceDirect

Materials Science for Energy Technologies

journal homepage: www.keaipublishing.com/en/journals/materials-science-for-energy-technologies

A comprehensive study of binder polymer for supercapattery electrode based on activated carbon and nickel-silicon composite

Markus Diantoro [a,b,*], Istiqomah Istiqomah [a], Oktaviani Puji Dwi Lestari [a], Yusril Al Fath [a], Yudyanto Yudyanto [a], Chusnana Insjaf Yogihati [a], Munasir Munasir [c], Diah Hari Kusumawati [c], Zarina Binti Aspanut [d]

[a] Department of Physics, Faculty of Mathematics and Natural Science, Universitas Negeri Malang, Malang 65145, Indonesia
[b] Center of Advanced Materials for Renewable Energy, Universitas Negeri Malang, Malang 65145, Indonesia
[c] Department of Physics, Faculty of Mathematics and Natural Science, Universitas Negeri Surabaya, Surabaya 60231, Indonesia
[d] Department of Physics, Faculty of Science, University of Malaya, Kuala Lumpur 50603, Malaysia

ARTICLE INFO

Article history:
Received 30 December 2022
Revised 16 March 2023
Accepted 18 March 2023
Available online 21 March 2023

Keywords:
Binder
Activated Carbon
Nickel
Silicon
Supercapacitor
Battery
Supercapattery

ABSTRACT

Current trends suggest that as manufacturing and energy demand increase, there will be a greater consumtion for energy storage, requiring its utilization for days, weeks, or even months in the future. Recent studies also need to be conducted on binders that could support electrode performance, considering that binders are also a crucial component of the electrochemical processes in cells. In this study, activated carbon-based supercapacitor electrodes were fabricated using three different binders: PVDF, SBR, and LA133. With a gravimetric capacitance and power density of 52.57 Fg^{-1} and 92.64 $W.kg^{-1}$, and a lifetime up to 87.23% after 1000 cycles, AC/CB LA133 has the best performance. LA133 was used as a binder to generate a Ni/Si composite as a battery electrode combined with the AC/CB LA133 supercapacitor to fabricate a supercapattery. This clearly shows that when a suitable binder such as LA133 is used, the electrochemical performance could be improved.

© 2023 Published by Elsevier B.V. on behalf of KeAi Communications Co., Ltd. This is an open access article under the CC BY-NC-ND license (http://creativecommons.org/licenses/by-nc-nd/4.0/).

1. Introduction

The demand for energy technologies in modern society has been steadily rising over the past few years because of the growing pressure on energy consumption [1]. Fossil fuels are now extensively used worldwide, but they have caused a number of issues collectively known as the energy crisis [2]. Owing to the continual use of non-renewable fossil fuels and concerns about global warming, the proportion of the world's electricity demand is changing dramatically [3]. Hence, there is a great concern to manufacture affordable and environmentally friendly materials for high-performance energy storage devices because the general public is going to face many risks, such as climate change, depletion of resources, and environmental carbon emissions [4]. Innovative technologies that are already used, such as electric vehicles (EVs), help to minimize electricity costs and optimize energy consumption [5] and home energy management systems (HEMS), which focus on regulating and controlling energy consumption in houses [6]. Therefore, the principles of both systems have led to the development of various energy storage technologies, including supercapacitors, batteries, fuel cells, and ultracapacitors [7–10].

The fundamental components of an energy storage device are - two electrodes (cathode and anode), which are separated by a separator, and an electrolyte (a substance that conducts ions but is electrically insulating, forms in solid, aqueous, and gel forms) [11]. To ensure that the electrode material sticks to the current collector during the charge–discharge process, these electrodes are typically fabricated using several binders. The binder is an important part of an energy storage system because a compact framework of the active material is required for energy storage to exhibit good physical and chemical properties [12]. Some binders used in energy-storage devices are polyvinylidene fluoride (PVDF), carboxymethyl cellulose (CMC), styrene butadiene (SBR), and polyacrylic latex (LA133) [13–15]. Thus, it is crucial to choose the appropriate binder to ensure that energy storage devices perform well.

Electrodes are essential components of energy storage systems. They primarily consist of materials with good electrical properties and stability [16], low cost [17], wide availability [18], and high

* Corresponding author at: Department of Physics, Faculty of Mathematics and Natural Science, Universitas Negeri Malang, Malang 65145, Indonesia.
E-mail address: markus.diantoro.fmipa@um.ac.id (M. Diantoro).

https://doi.org/10.1016/j.mset.2023.03.005
2589-2991/© 2023 Published by Elsevier B.V. on behalf of KeAi Communications Co., Ltd.
This is an open access article under the CC BY-NC-ND license (http://creativecommons.org/licenses/by-nc-nd/4.0/).

redox reaction materials [19]. Many energy storage systems use activated carbon because of its high specific surface area [20], hierarchical porous structure [21], and high physical and chemical stabilities [22]. Activated carbons are used as supercapacitor electrodes to ensure unhindered ion transport at rapid charge–discharge rates because of their large surface area for electrolyte ion adsorption and readily accessible pore structure [23]. Based on the ion adsorption between the electrode and electrolyte interface, activated carbon exhibits the behavior of Electric Double Layer Capacitor (EDLCs) [24]. Micropores and rod-like activated carbon electrodes exhibited a specific capacitance of 365F.g^{-1}, with an ultra-high power density of 600 W.kg^{-1} and could maintain up to 94.8% capacitance after 10,000 cycles [25]. The fast charge/discharge (high power density) and extremely long cycle life of activated carbon electrodes is one of the major characteristics of supercapacitors [26–29].

On the other hand, batteries have emerged as the most captivating energy technology owing to their high energy density [30], flexibility [31], ease of handling[32] and long life time stability [33]. One of the most impressive anode materials for the upcoming generation of lithium-ion batteries is silicon, which has been extensively studied because of its incredibly high theoretical capacity (4200 mAh.g^{-1}) [34], low potential (0.4 V vs. Li/Li^{+} [35], and widespread availability [36]. Silicon (Si) has been hailed as one of the most significant near-term advances in Li-ion battery technology to replace graphite, resulting in a higher energy density [37]. The self-healing binder and even a silicon anode demonstrate superior electrochemical performance and outstanding high stability, delivering a high discharge capacity of 3744 mAh.g^{-1} at a current density of 420 mA.g^{-1} and facilitating a stable cycle life with a high capacity retention of 85.6% after 250 cycles at a high current rate of 4200 mA.g^{-1} [38]. However, the commercial use of silicon materials is significantly hindered by the significant volume change that occurs in silicon during cycling [39]. This volume change results in irreversible capacity loss and the destruction of the electrode structure [40]. Numerous approaches have been proposed in recent years to address the drawbacks of Si.

Nickel (Ni)-based materials are considered potential candidates for energy storage devices because of their distinct performance characteristics, inexpensive[41], incredible amount [42], and high capacity [43]. Nickel is fiercely competitive but is frequently ignored. Ni metal can be managed without additional safety precautions because it is chemically stable in both air and water [44,45]. The highest volumetric capacity was obtained for nickel (8136 mAh cm^{-3}. For thermal safety, particularly in the event of short circuits in large-scale energy storage devices, its high melting point is advantageous. More importantly, nickel is not likely to produce nickel salts or dendrites as by products [46]. The electrochemical capacity of nickel-doped mWO_3 is 1287/1012 mAh.g^{-1} at 100 mA.g^{-1}, and it has a good cycle life (capacity retention of 79.60% after 500 cycles) and rate capability (650.2 mAh.g^{-1}) even at larger current densities (1000 mA.g^{-1}) [47].

In this study, Ni-Si-based composites were generated as battery electrodes, with the potential advantages of both materials and their respective drawbacks. The Ni-Si composite was used as the anode (representing high energy density as a characteristic of battery) and activated carbon was used as the cathode (representing high power density as a beneficial supercapacitor). Thus, the combination of these two systems can produce a high-performance device known as supercapattery. Supercapattery, which integrates the beneficial performances of both batteries and supercapacitors, was introduced in 2011. The creation of a hybrid device has the advantage of producing high energy by combining a battery-type material with the ability to deliver high power from supercapacitor-type materials. Supercapattery devices are considered suitable as energy sources for scalable and self-recharging leadless implantable devices because the combination of the two mechanisms may increase the cell voltage and enhance the cell lifetime. This report demonstrates the possibility of using supercapatteries in implantable devices. With such remarkable characteristics, efficient electrode materials are still required to enhance the supercapacitor performance. A supercapattery formed of Ni@Cu/WS_2 as the positive electrode and activated carbon as the negative electrode achieved a specific capacity of 185.8C/g, showing a high energy density and power density of 439 Wh/kg and 425 W/kg, respectively [48]. In another study, Ni manganese sulfide was combined with activated carbon to design a supercapattery (Ni–Mn–S/AC). This combination produced a high capacity (420.10C/g) with the highest energy density of 75.96 Wh/kg [49].

The reported data encourage further insightful research in the area of energy storage. Therefore, a comparison of various binders, including PVDF, SBR, and LA133, which are used as binder-activated carbon supercapacitor electrodes, was conducted in this work. Supercapattery will be fabricated by using carbon based as anode and Ni-Si as cathode [50]. The optimum performance binder will be used as the negative electrode of the supercpattery, with the Ni-Si composite as the positive electrode. The supercpattery's electrochemical performance will also be evaluated using a variety of structural and physicochemical characterizations. Practical implementation of a proper binder, good electrode material, and a suitable electrolyte can result in energy storage devices with high electrochemical performance.

2. Materials and methods

2.1. Materials

The chemicals used The chemicals used in this work (from multiple companies) were of analytical grade and used without purification: activated carbon (AC, CGC, Bangkok, Thailand), carbon black (CB, Imerys, La Hulpe, Belgium), Silicon and Nickel (Si and Ni, Sigma Aldrich, Burlington, MA, United States), polyvinylidene fluoride (PVDF, Sigma Aldrich, Burlington, MA, United States), dimethylacetamide (DMAc, Sigma Aldrich, Burlington, MA, United States), styrene butadiene (SBR, Alibaba, China), acrylic latex (LA133, Alibaba, China), tetraethylammonium tetrafluoroborate (Et_4NBF_4, Gelon, Shandong, China), acetonitrile (ACN, Merck, Darmstadt, Germany), and deionized water. Coin cells set were purchased from a TOB machine (Fujian, China).

2.2. Synthesis of activated carbon supercapacitor electrode

The activated carbon electrode was prepared using a simple mixing method with a mass ratio of the active material (activated carbon), conductive material (carbon black), and binder of 8:1:1. Initially, PVDF was dissolved in dimethylacetamide (DMAc), while SBR and LA133 were dissolved in deionized water to form a white solution. The binder solution was stirred for 1.5 h to ensure that no bubbles formed during mixing. Activated carbon and carbon black were then added to the binder solution to form a paste electrode. The electrode paste was deposited on an aluminum foil substrate using a Dortor blade and dried at 50 °C for 24 h.

2.3. Synthesis of Ni-Si composite for battery electrode

Along with the supercapacitor electrode, Ni-Si composite was synthesized by a simple mixing method with a mass ratio of active material (Ni (80%), Si(20%)), conductive material (carbon black), and binder (LA133) of 8:1:1. LA133 was dissolved in deionized water for 1.5 h to obtain a binder slurry, which was then gradually filled with active and conductive materials. The resulting paste was

stirred at room temperature. The nickel foam substrate was sonicated with alcohol for 1 h and dried at 100 °C 1 h. The paste was then deposited onto the nickel foam using a micropipette with volume of (20 μL) for all variations. The electrodes were dried for an hour in an oven at 100 °C.

2.4. Assembly of the supercapacitor and supercapattery devices

The active material mass loadings (areal density) of each electrode in different binder is significantly lower than 10 mg/cm^2. AC electrode in three different binder of LA133, SBR, PVDF has areal denisty of 5.73 mg/cm^2, 5.41 mg/cm^2, 6.05 mg/cm^2 respectively. The AC electrode was cut into a circle with a diameter of 2 cm, while the Ni-Si electrode was pressed and soaked in an organic electrolyte 1.0 M Et_4NBF_4 for 24 h. After all electrodes were prepared, a supercapacitor and supercapattery was fabricated. Supercapacitor was fabricated by arranged two AC electrode symmetricly. In another hand, An AC electrode was used as the negative electrode and a Ni-Si composite was used as the positive electrode for fabricated supercapattery. Both electrodes were placed in coin cells (LIR2032) along with a cloth fiber separator. A small amount of 1.0 M Et_4NBF_4 and pressed. The cell was ready for measurement using electrochemical equipment.

2.5. Characterization

An X-Ray diffractometer (XRD, PAN Analytical X'Pert PRO, Malvern Panalytical, Worcestershire, United Kingdom) and Raman

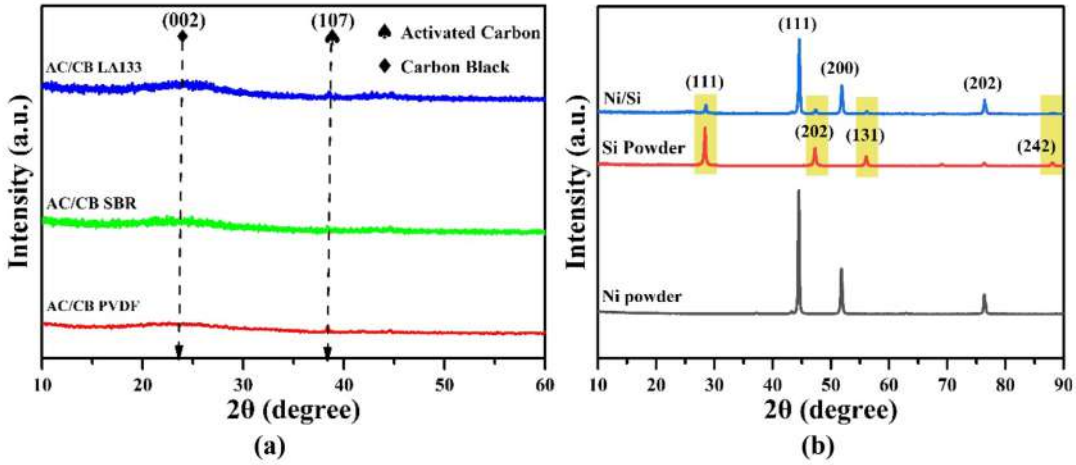

Fig. 1. X-ray diffraction patterns of (a) Activated carbon thin film electrode in various binder (LA133, SBR, PVDF), and (b) Ni, Si and Ni/Si powder composite.

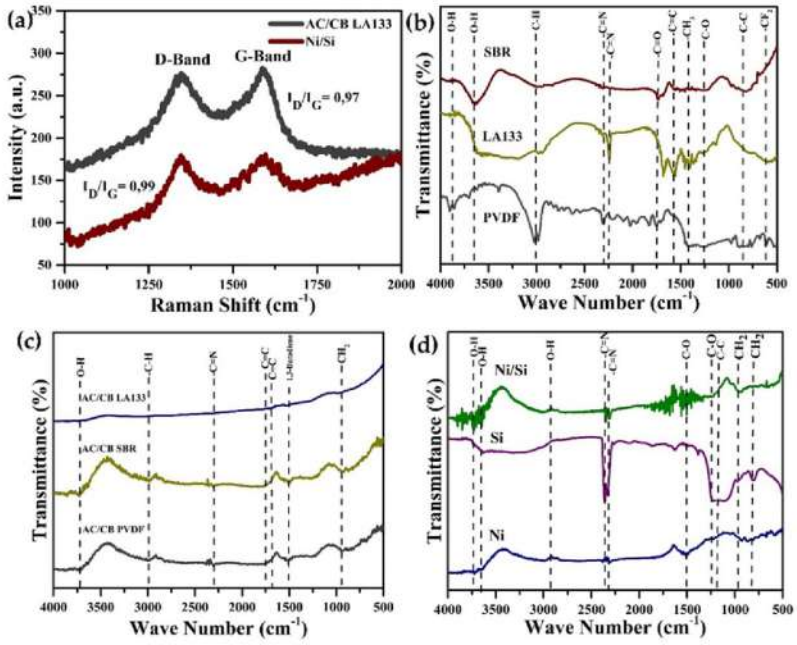

Fig. 2. (a) Raman spectra of AC/CB LA133 and Ni/Si composites, (b) FTIR spectra of SBR, LA133 and PVDF binder, (b) Activated carbon electrodes using different binder, (c) Ni, Si and Ni/Si composite.

spectrometer were used to characterize the structural information of each material. Scanning electron microscopy (SEM, Inspect S50, FEI Company, Hillsboro, OR, USA) was used to analyze the morphology of the film electrode and Ni and Si powders. Nitrogen adsorption and desorption at 77 K with ASAP2460 (Micromitics, Hexton, United Kingdom) and Quantachrome 3.0 were used to characterize the porous structures of each material and film composite. The multi-point Brunauer-Emmett-Teller (BET) method and Barrett–Joyner–pore Halenda (BJH) size distributions were used to calculate the specific surface area (BJH). Cyclic voltammetry (CV) and electrochemical impedance spectroscopy (EIS) were performed for electrochemical measurements in a two-electrode system (PGSTAT302N, Metrohm, Herisau, Switzerland). The voltage window for the CV measurements was 0–2 V, and the scan rate ranged from 10 to 100 $mV.s^{-1}$. A frequency range of 100 kHz to 10 MHz was used for the EIS analysis. Galvanostatic charge–discharge was another factor that defined the electrochemical performance (GCD, BTS4000, Neware, Shenzhen, China). GCD cycles were performed with cutoff voltages ranging from 0 to 2.6 V and current densities ranging from 0.1 to 1.5 Ag^{-1}, GCD cycles were performed.

2.6. Calculation

The crystal size is obtained using the Debye-Scherrer equation, which is expressed in equation (1):

$$D = \frac{K\lambda}{\beta cos\theta} \tag{1}$$

where D is the size of the crystal in nanometers, K is the form factor, λ is the wavelength of the XRD graph, β is the FWHM generated from the XRD graph, and θ is the Bragg angle.

Afterwards, the surface area determined by BET measurement was calculated using Equation (2) from the t-plot method [[51]]:

$$\frac{x}{W[1-x]} = \frac{1}{C \times W_{ml}} + \left[\frac{C-1}{C \times W_{ml}}\right]x \tag{2}$$

W_{ml} is the mass of adsorbate required to form a complete monolayer on a specific sample, where W is the mass adsorbed at the relative vapor pressure and x = P/Po (P and Po are the actual and saturated vapor pressures of the adsorbate, respectively). The heat of adsorption differences between the first and second or higher layers are expressed by the constant C, which is temperature- and first-layer heat of adsorption-dependent.

The gravimetric capacitance (C, $F.g^{-1}$) was determined by calculating from the galvanostatic charge–discharge using Equation (3) [[52,53]]:

$$C = \frac{4I\Delta t}{m\Delta V} \tag{3}$$

where I is the constant discharge current (A), Δt is the discharge time (s), m is the mass of the active material (g) on the two electrodes, and ΔV is the voltage difference (V) excluding the ohmic (IR) drop.

The gravimetric specific energy density (E, Wh kg^{-1}) and power density (P, $W.kg^{-1}$) of the cells were calculated using Equations (4) and (5), respectively [[52,53]]:

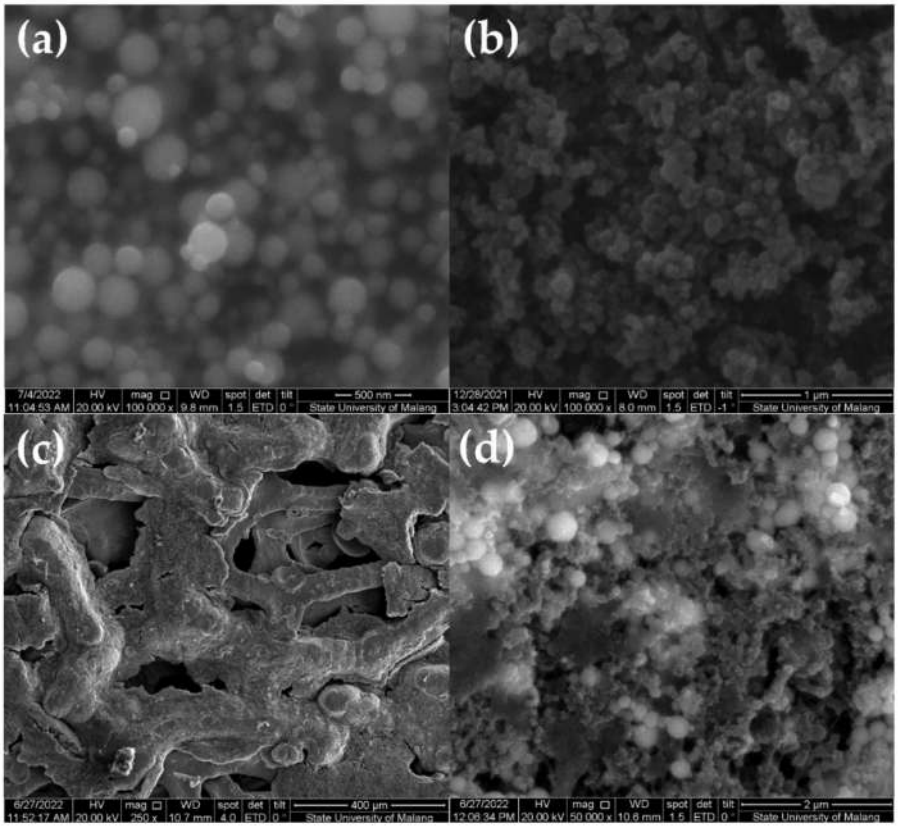

Fig. 3. SEM image of (a) Nickel (100.000x), (b) Silicon (100.000x), (c) Ni/Si deposited on nickel foam substrat (250x) and (d) Ni/Si electrode surface morphology (50.000x).

$$E = \frac{1}{8}\frac{C\Delta V^2}{3.6} \quad (3)$$

$$P = \frac{E \times 3600}{\Delta t} \quad (4)$$

where C is the gravimetric specific capacitance of the cell, ΔV is the voltage change during the discharge process after the IR drop, and Δt is the discharge time (s).

3. Results and discussion

The structure, size, and phase of the materials were examined using XRD using Cu-Kα radiation with a wavelength of 1.54060 Å and a diffraction angle range of 10 °to 90°. Fig. 1**a** shows a graph of the diffraction patterns of activated carbon electrodes with different binders. The amorphous structure indicates the activated carbon dominates the film electrode. The peaks of activated carbon diffraction are shown at 2θ = 65° and 78.49° associated to the respective Bragg's planes of (122) and (220) [54,55]. The high specific surface area and specific capacitance of activated carbon are both a result of its amorphous structure [56].

Ni, Si, and thin films of Ni/Si composites generated diffraction patterns, as shown in Fig. 1**b**. Ni peaks exist with the Bragg's plane of (111), (200), and (202), in accordance with 2θ = 28.49°, 44.56°, 51.92°, and 77.04° (JCPDS 04–850). On the other hand, the existing silicone is indicated by (111), (202), (131), and (242) planes at 2θ of 28.49, 47.35°, 56.19°, and 88.11°, respectively (JCPDS 27–1402). Lower intensity diffractions the comoposite were obtained when comparing the Ni/Si thin films to those made of pure Si and pure Ni. These peaks reduction may caused by a small amount of amorphous phases of binder and other conductive material such as carbon black [57]. The crystal sizes of Ni, Si, and Ni/Si were calculated based on the Debye-Scherrer on equation 1. However, the crystal size of Si nanoparticle's is 13.4 nm, nickel nanoparticles is 14.82 nm and the crystal size rises to 15.4 nm when the both are combined to generate a Ni/Si composite. Commercial Si has a slightly smaller crystal size (26–330 nm) than self-synthesized Si [58]. Ni also has a crystal size smaller than 20 nm when produced by $NaBH_4$ synthesis [59]. The performance of supercapacitors may be impacted by considering an ideal electrode with an appropriate crystalline size. The performance of supercapacitors is significantly enhanced by their small crystal size. The smallest ZnO crystalline size, 15 nm, showed significant reductions in charge transfer resistance compared to bulk ZnO (0.5 μm), resulting in good fardic behavior [60].

The Raman spectra of the AC-CB LA133 and Ni-Si composites are shown in Fig. 2**a** at characteristic peaks of 1345.5 cm^{-1} and 1597 cm^{-1}, where the D band contains Sp^2 carbon and the G band contains Sp^3 carbon [61,62]. The structural level of the graphic structure was evaluated using the integral ratio (I_D/I_G) [63]. The ratios of the Ni-Si composite and the AC-CB LA133 are 0.97 and 0.99, respectively. Additionally, Ni-Si performed better because it had a higher level of graphitization based on the I_D/I_G ratio.

The absorption functional groups of the binder variations shown in Fig. 2**b** are identified using FTIR measurement. O-H func-

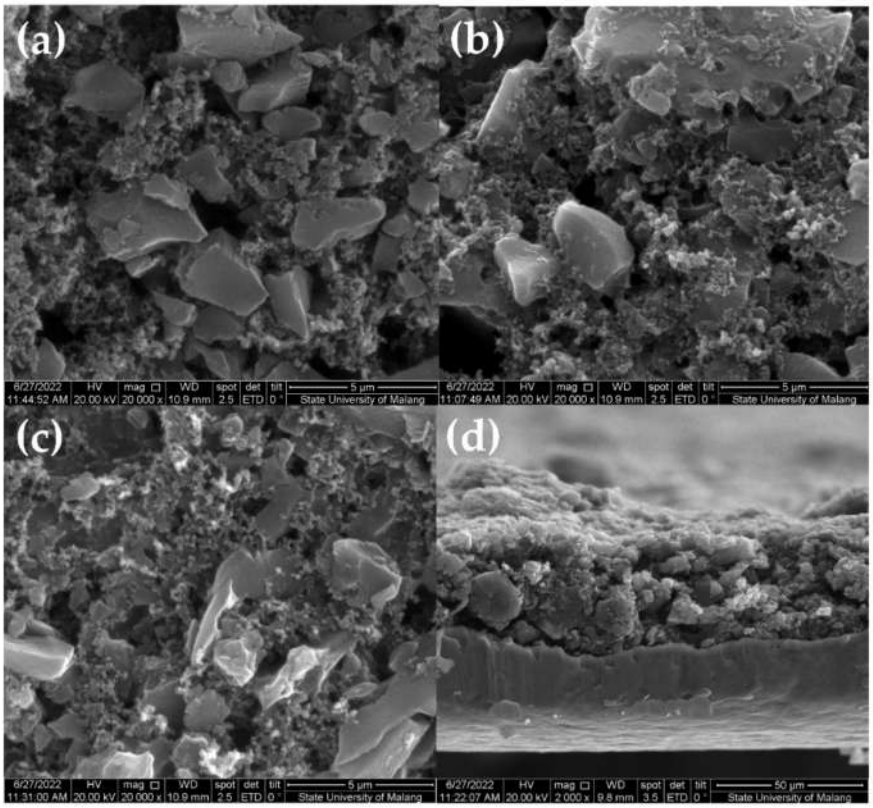

Fig. 4. Surface morphology in the 20.000x magnification of activated carbon electrode in different binder (a) PVDF, (b) SBR, (c) LA133, and electrode cross section morphology (2000x).

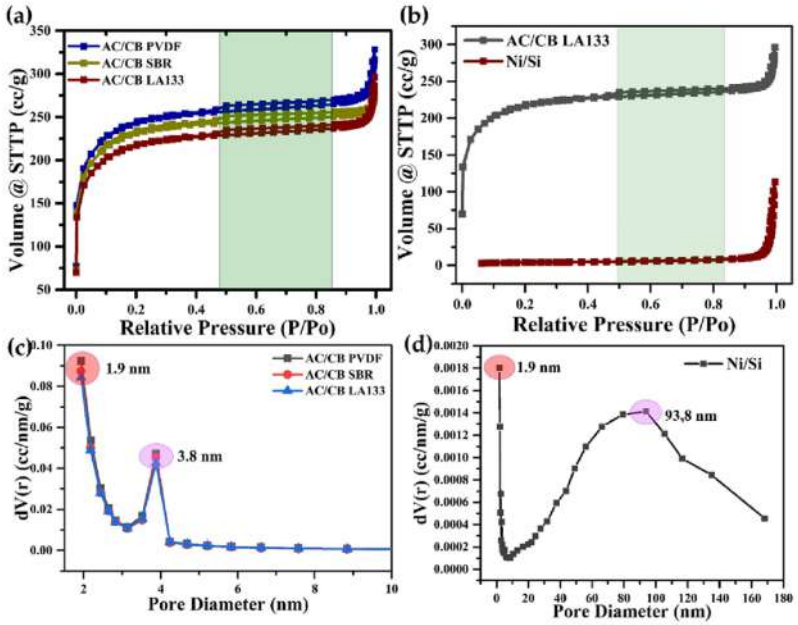

Fig. 5. N_2 adsorption–desorption isotherm curve of (a) activated carbon electrode in various binder, (b) AC/CB LA133 compared to Ni/Si composite, (c) pore distribution of each AC/CB electrode, and (d) Ni/Si.

Table 1
The BET parameter of AC/CB and Ni/Si composite (syrface area, pore volume and pore size).

Sample	S_{BET}(m^2g^{-1})	V_{total} (cm^3g^{-1})	Pore Size (nm)
AC/CB PVDF	894.69	0.49	3.87
AC/CB SBR	851.84	0.42	3.87
AC/CB LA133	787.43	0.45	3.87
Ni/Si	13.05	0.15	93.87

tional groups are present in PVDF binders with a wave number of 3880.87 cm^{-1}, C-H functional groups with a wave number of 3000 cm^{-1}, C-N functional groups with a wave number of 2294.57 cm^{-1}, C=O functional groups with a wave number of 1746.59 cm^{-1}, and CF_2 functional groups with a wave number of 606.06 cm^{-1} [64]. Wave numbers for the SBR binder include 2250 cm^{-1} for a CN functional group, 1580.58 cm^{-1} for a C=C functional group, and 1421.49 cm^{-1} for a CH_3 functional group [65]. The LA133 binder, on the other hand, has wave numbers of 3651.84 cm^{-1} for an O-H functional group, 1746.59 cm^{-1} for a C=O functional group, 1262.4 cm^{-1} for a C-O functional group, and 842 cm^{-1} for a C-C functional group [66].

Fig. 2**c** shows the absorption function of the thin film on the AC-CB cathode electrode. The O-H functional group in AC-CB PVDF has a wave number of 3727.93 cm^{-1}, the C-H functional group has a wave number of 3000 cm^{-1}, the C-N functional group has a wave number of 2300.72 cm^{-1}, the C = C function group has a wave number of 1752.74 cm^{-1}, the 1.3-butadiene functional group has a wave number of 1500 cm^{-1}, and the CH_2 functional group has a wave number of 943.45 cm^{-1} [67]. The O-H functional group in AC-CB SBR has a wave number of 3727.93 cm^{-1}, the C-H functional group has a wave number of 3000 cm^{-1}, the C-N functional group has a wave number of 2300.72 cm^{-1}, the 1,3-butadiene functional group has a wave number of 1500 cm^{-1}, and the CH_2 functional group has a wave number of 943.45 cm^{-1} [68]. In contrast, the wave numbers for AC-CB LA133 are 1682.8 cm^{-1} for the functional group C=C and 943.45 cm^{-1} for the functional group CH [69].

The absorption functional groups observed in the Ni-Si anode thin films are shown in Fig. 2**d**. Ni has wavenumbers of 1500 cm-1 for the functional group C-O and 3734.07 cm^{-1} for the functional group O-H [70]. Si has a wavenumber of 3644.92 cm^{-1} with a functional group of O-H, a wave number of 2358.36 cm^{-1} with a functional group of C-N, a wave number of 1192.46 cm^{-1} with a functional group of C-C, and a wave number of 809.72 cm^{-1} with a functional group of CH_2 [71]. Ni-Si has wave numbers of 3000 cm^{-1} for an O-H functional group, 2319.93 cm^{-1} for a C-N functional group, 1268.55 cm^{-1} for a C-O functional group, and 937.3 cm^{-1} for a CH_2 functional group [72].

SEM was used to examine the surface morphology. Fig. 3 depicts the surface morphology of the Ni, Si, and Ni/Si composites deposited on the nickel foam. Ni particles with an average size of 140.54 nm are represented in Fig. 3**a** as perfectly spherical. In addition, the Ni particles behave a disperse type. The results are in line with earlier research, which suggests that nickel powders ground in planetary ball mills have a range of particle sizes between 53.8 and 183.2 nm [73]. The Si particles in Fig. 3**b**, in contrast to the Ni particles, appear to be slightly agglomerated in several areas. Si is not perfectly spherical in shape with an average particle size of 55.43 nm. The results for Si particle size are consistent with those of Si for wastewater treatment, which suggests that the Si particle distribution ranges from 200 to 800 nm [74]. The surface morphology of the electrode after the Ni/Si composite was formed and deposited on a nickel foam substrate as a supercapattery positive electrode material is shown in Fig. 3**c**. The Ni/Si composite paste barely covered the Ni foam pores, which were clearly discernible. The pores of nickel foam provide many advantages, such as mechanical flexibility [75], high porosity in electrolyte ion absorption [76], rapid electron transport, and fast ion diffusion [77]. When Fig. 3**c** is magnified up to 50,000× and transformed into Fig. 3**d**, the electrode surface can be observed more clearly. Therefore, different components of the electrode were easily visi-

ble. The spherical shape of the Ni particles makes them observable. The conductive material, carbon black, is uniformly distributed with respect to Ni and Si.

The SEM images in Fig. 4 show the surface morphologies of the activated carbon electrodes with different binders. Fig. 4**a–c** does not appear to be significantly different from each other. The activated carbon bulk and binder particles differ significantly, even though different binders are used. The activated carbon was uniformly covered by a binder. The electrode paste was homogenously deposited with a thickness of 36.55 μm, as shown in Fig. 4**d**.

Porosity is an important factor that determines the electrochemical performance of a sample. Porosity of the materials interconnected with electrolyte would affect the supercapacitor's ability to store energy [78,79]. The performance of supercapacitors can be improved by increasing the pore size of the material [80]. Moreover, the effectiveness of an electrode can be affected by the electrolyte used [81]. The electrochemical performance that occurs within the cell will be faster and more efficient if the size of the ion electrolyte and the pore size of the electrode material are suitable. Therefore, measurements of nitrogen adsorption and desorption on composite film electrodes are necessary. Fig. 5**a, b** shows the adsorption–desorption isotherm curves of the AC/CB electrode for various binders and Ni-Si composite electrodes. According to the International Union of Pure and Applied Chemistry (IUPAC) classification, the AC/CB electrode isotherm curve (Fig. 5**a** indicates a type IV classification for typical mesoporous materials [82]. Compared to the Ni-Si composite electrode, the isotherm curve in Fig. 5**b** exhibits a type III classification with typical macropore materials [83]. Micopores were indicated by the AC/CB electrode at moderate relative pressures (P/P0 = 0.5–0.8) [84]. Additionally, a relatively high increase in isotherm adsorption (P/ P0 = 0.9–1.0) indicated athe lack of macropores [85]. The Ni-Si composite (P/P0 = 0.5–0.8) at moderate relative pressure indicates the presence of mesopores [86]. In contrast, a relatively large increase in isotherm adsorption (P/P0 = 0.9–1.0) indicated the absence of macropores [87].

Fig. 5**c, d** displays the pore size distribution of the two samples. The identical 3.87 nm pore size of AC/CB demonstrates that the pore size is mesoporous (>2 nm). In contrast to AC/CB, the Ni/Si composite has a pore size of 93.87 nm, belonging to the macropore pore size (>50 nm) [88]. Furthermore, there are significant differences in the surface area and the pore volume as list on Table 1. The surface area of AC/CB, calculated by equation 2, ranges from 787.43 to 895.69 m^2g^{-1}. While the surface area of the Ni/Si composite is much lower, at 13.05 m^2g^{-1}. This distinguishes both as being very different. A large surface area can exhibit lots of active sites [89], and shorten the ionic transfer path and enable rapid capacitive ion storage [90]. The statement that a supercapacitor has a high-power density with excellent electrochemical performance is supported by the large surface area of AC/CB. On the other hand, even though Ni and Si are battery materials that have been widely used, judging from their surface area, it is necessary to combine them with other materials, including AC/CB to get good electrochemical performance. This is the main principle of the supercapattery, which combines batteries and supercapacitors with their complementary benefits and drawbacks.

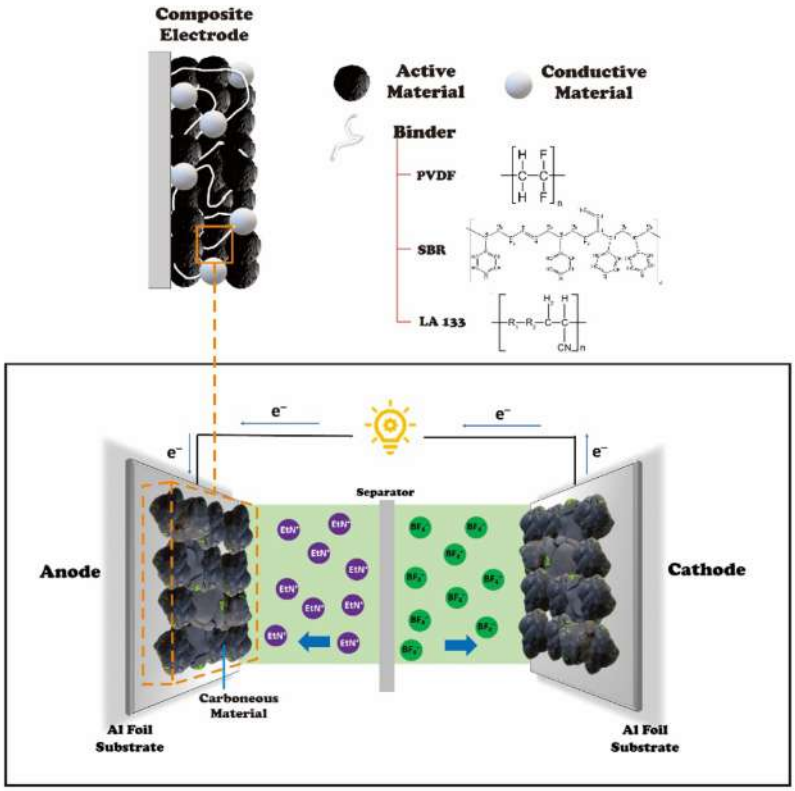

Fig. 6. Schematic illustration of AC/CB supercapacitors electrode with various binder (PVDF, SBR, LA133) and the EDLC mechanism.

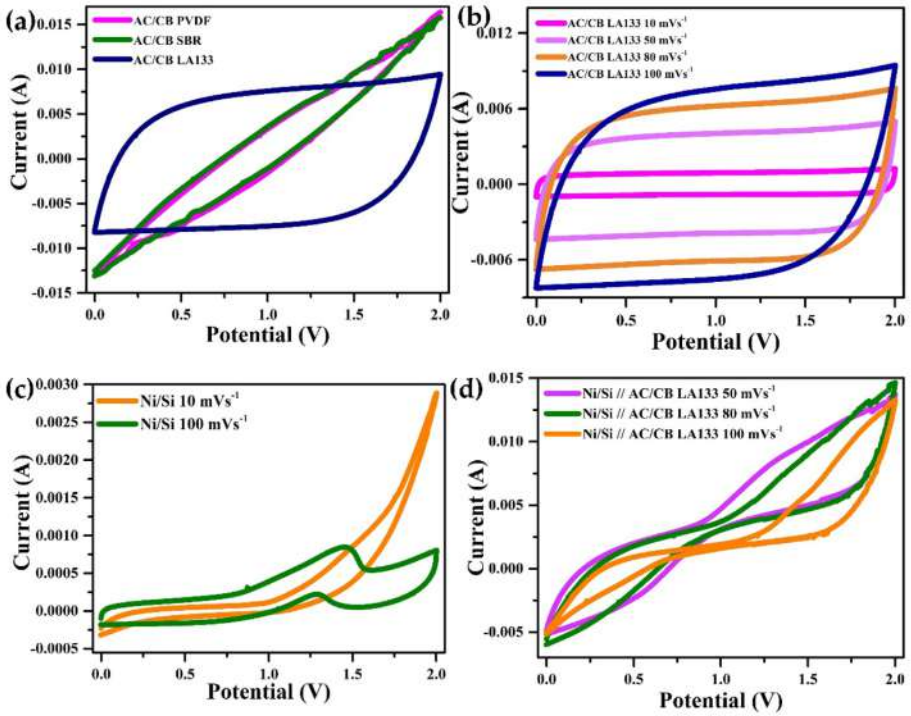

Fig. 7. Cyclic voltammetry curve of (a) AC/CB PVDF, SBR, LA133, (b) AC/CB LA133 at a scan rate of 10, 50, 80, 100 mVs^{-1}, (c) Ni/Si composite at a scan rate of 10 and 100 mVs^{-1}, (d) supercapattery Ni/Si // AC/CB LA133 at a scan rate of 50, 80, 100 mVs^{-1}.

The electrochemical performance of supercapacitors can be determined by conducting a two-electrode system in a coin-cell device. The equipment used included cyclic voltammetry and galvanostatic charge/discharge. Cyclic voltammetry measurements were performed at a voltage of 0–2 V at scan rates of 10, 50, 80 and 100 mVs^{-1}. The CV curves of the supercapacitor electrodes AC/CB in several binders and supercapattery Ni/Si // AC/CB LA133 with a voltage in the range of 0–2.0 V are shown in Fig. 7. With a scan rate modification of 10 to 100 mVs^{-1} (Fig. 7**a**, the AC/CB LA133 demonstrated a semi-rectangular (quasi-rectangular) CV curve, whereas the AC-CB PVDF and SBR did not exhibit the square shape typical of supercapacitors [91]. The semirectangular CV shape represents one type of supercapacitor: the electric double-layer capacitor (EDLC). This is because carbon materials, which are present in EDLC materials as shown in Fig. 6, make up the majority of the electrode composition [92]. Even though all three are composed of carbon, a very noticeable difference can be seen in the area of the CV curve. Compared with AC/CB PVDF and SBR, which have almost the same CV curve area, AC/CB LA133 has a much larger CV curve area. The specific capacitance increased as the area of this curve increased, suggesting that the electrode could store more charge [93]. At scan rates of 50–100 mVs^{-1}, shown in Fig. 7**b**, the curve is remarkably well built and uninterrupted, indicating an increase in electron conduction in the electrode that supports rapid charge diffusion and, as a result, excellent and stable capacitive performance [94,95]. However, as the scan rate increased, a change in shape was observed from the entire curve. The semi-quasi-rectangular shape was sustained at scan rates of 10 and 20 mVs^{-1}. Because of insufficient electrolyte ion diffusion, the curve is more likely to point at the tip when the scan rate is between 50 and 100 mVs_{-1} [96,97]. Because of the inability of electrolyte ions to enter the pores of the active material at high scan rates, the electrochemical reaction screws up [98]. According to the CV results, the AC/CB LA133 electrode significantly outperformed other electrodes. Therefore, the LA133 AC/CB electrode was used as the negative electrode of the supercapacitor, as the representative side of the supercapacitor. Utilizing AC/CB LA133 as the cathode provides high power density because of the electrical double layer that expands between the electrolyte and activated carbon [99].

The supercapattery battery-side electrodes were made of a Ni/Si composite, and their CV curves are shown in Fig. 7**c**. Compared to the previous carbon-based CV curve, the Ni/Si composite CV curve had a significantly different shape. The battery CV curve has a redox shape with peaks similar to those shown in Fig. 7**c**, which is characteristic of the battery material [100]. CV tests were carried out at various scan rates (from 10 to 100 mVs^{-1}) over a potential range of 0–2.0 V to further compare the electrochemical kinetic properties of the supercapattery Ni/Si // AC/CB LA133 (Fig. 7**d**). Following increases in the scan rates, peak shifts can be observed in the CV curves in relation to the tw samples. These characteristics indicate polarization of the electrode [101]. In the analysis of the CV curves of supercapattery Ni/Si / AC/CB LA13, a high current response was observed along with two redox peaks, which were primarily caused by the Faradaic response of the electrodes in the as-developed state in the aqueous electrolyte solution, which corresponded to the material's typical battery-like behavior. It was observed that as the scan rate was increased, the current response exhibited uniform CV curve shapes, demonstrating the excellent reversibility of the active electrodes with battery-like capabilities during the faradaic reaction [102]. These reactions occur when the working electrode interacts with the electrolyte ions. The two wider peaks, which show oxidation and reduction peaks, indicate that their redox potentials are close to

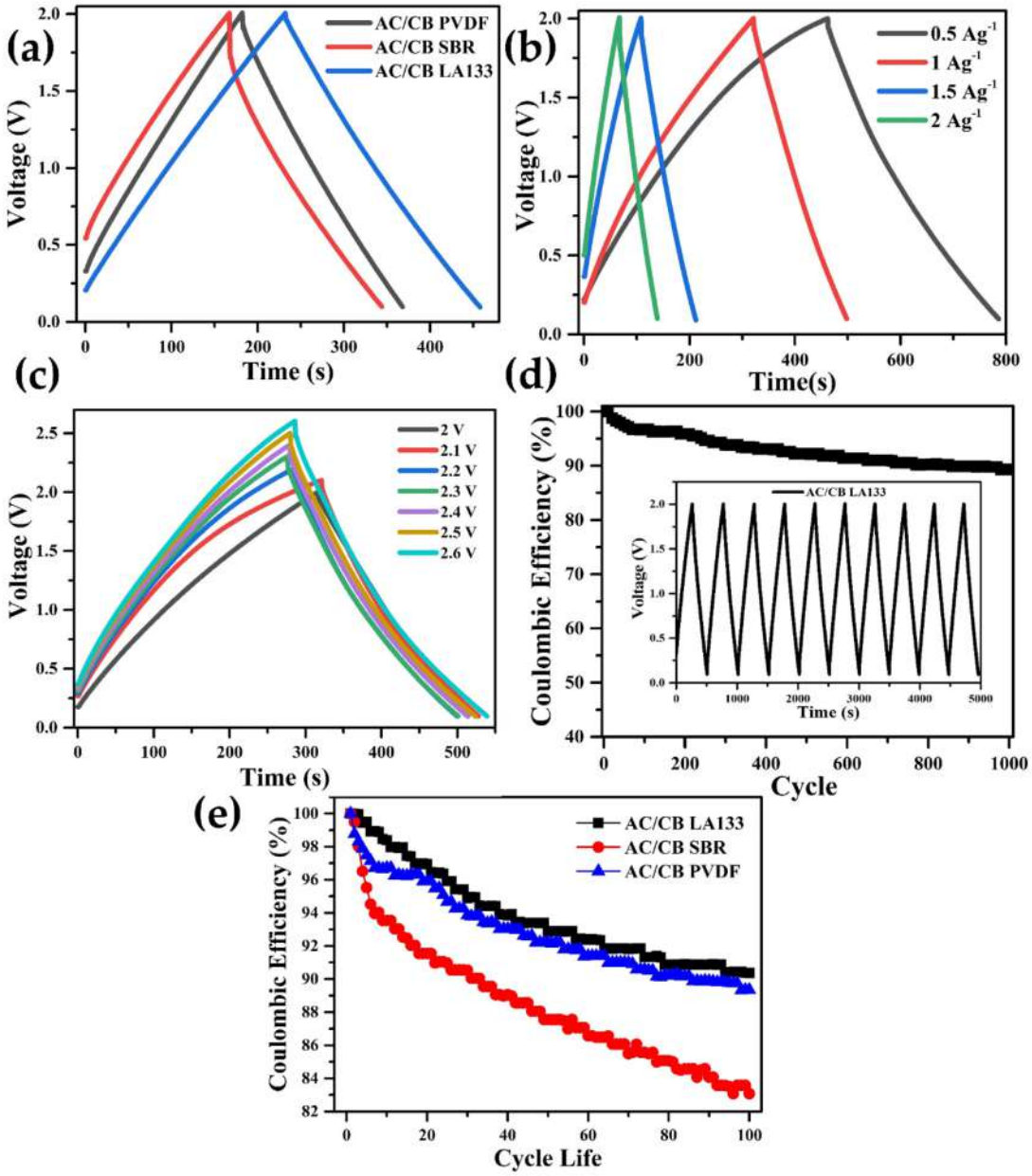

Fig. 8. (a) Charge discharge behavior of AC/CB PVDF, SBR, LA133 at 2 V potential window, (b) AC/CB LA133 at various current density range from 0.5 to 2 Ag^{-1}, (c) different potential window (2–2.6 V), (d) retention at 1 Ag^{-1} for 1000 cycles, (e) coulombic efficiency of activated carbon based in varous binder.

one another. The shift in the horizontal and vertical peaks, which is inversely proportional to the increase in scan rate, can be used to determine the fast reaction rate of the electrode–electrolyte interactions [103].

The electrochemical performances of the supercapacitor and supercapattery devices were also evaluated using galvanostatic charge–discharge. All of the binders' AC/CB supercapacitor GCD curves in Fig. 8**a-c** exhibit a triangular shape that is particular to EDLC because activated carbon acts as the active component [104]. The triangle-shaped GCD curve demonstrates that the supercapacitor has good reversible charge–discharge stability [105]. Despite having the same shape, they differed in terms of discharge time. AC/CB LA133 has a discharge time of>500 s, which is longer than that of PVDF and SBR. According to equation 3, the discharge time is directly correlated with the gravimetric capacitance; therefore, the discharge time has an impact on the supercapacitor's performance. Therefore, the gravimetric capacitance increased as the discharge time increased.

The electrochemical performance parameter values for AC/CB-based supercapacitor devices with different binders in Table 2

Table 2
Comparative value of supercapacitors capacitance, energy density and power density.

Sample	Gravimetric Capacitance (Fg^{-1})	Gravimetric Energy Density ($Wh.kg^{-1}$)	Gravimetric Power Density ($W.kg^{-1}$)
AC/CB PVDF	44.19	4.99	90.30
AC/CB SBR	47.41	4.71	84.52
AC/CB LA133	52.57	6.27	92.64

show that the LA133 binder was the best binder. By calculating the electrochemical parameters (equation 3–5), AC/CB LA133 had the highest gravimetric capacitance of 52.57 Fg^{-1} with an energy density and power density of 6.27 $Wh.kg^{-1}$ and 92.64 $Wh.kg^{-1}$, respectively. In contrast, the performances of the AC/CB PVDF and SBR were still lower than that of LA133, with gravimetric capacitances of 44.19 Fg^{-1} and 47.41 Fg^{-1}, respectively.

Typically, the following factors contribute to the electrochemical loss of the electrodes: (1) the pulverization, over-charge, and discharge of electrode materials; (2) the formation of SEI films during the cycle process on the electrode surface; (3) decomposition of the electrolyte solvent during the discharge process; (4) irreversible side reactions because the electrode was unable to completely remove all; and (5) the slurry fell off the substrate after the charge–discharge cycles [106–108]. Here, the AC/CB PVDF electrode is expected to fall from the aluminum foil through the charge–discharge process. As reported in previous research, the $MnCo_2O_4$ electrode with PVDF as the binder showed poor cycle performance and was predicted to be impacted by the fifth factor above [109]. Polyvinylidene fluoride (PVDF) is the most widely used binder for electrodes because of its excellent electrochemical and thermal stability. PVDF's application of PVDF was constrained by some shortcomings such as the preference to swell at high temperatures and the necessity to dissolve in an organic solvent such as N-methyl-2-pyrrolidone (NMP), N,N-dimethylacetamide (DMAc), or N, N-dimethylformamide (DMF) [110]. The most typical organic solvent is known to be costly, volatile, combustible, toxic, poorly flexible, and poorly recyclable [111,112]. However, the unsaturated bond in SBR is oxidized at high potentials, making SBR unsuitable for use in cathode electrodes [113]. In contrast to PVDF and SBR, due of its lower cost, better solubility, and environmental friendliness, LA133 has been successfully used in the fabrication of electrodes [114,115]. It may also replace NMP with water, which provides the electrodes with excellent cycling ability and mechanical stability. The highest electrode was the AC/CB LA133 electrode, which may be a result of the LA133 binder's high concentration of polar –CN groups and strong intermolecular force. This feature of the LA133 binder is widely utilized in a variety of positive and negative materials [116].

AC/CB LA133 was subjected to various current densities, specifically in the range of 0.5–2 Ag^{-1}, generating the charge–discharge curve displayed in Fig. 8**b**. The narrower curve, which is defined by a faster discharge time, clearly shows the effects of different current densities. However, the shape of the curve is still triangular and does not change, indicating that the reversible electrochemical reaction takes place inside the cell [117]. In addition to various current densities, AC/CB LA133 was tested between 2 and 2.6 V potential windows. As a result, AC/CB LA133 maintained the triangular shape of the curve (Fig. 8**c**) while surviving up to 2.6 V. This typical behaviour was due to the organic electrolyte used as the electrolyte. Et_4NBF_4 is an organic electrolyte that has the advantage of producing a wider voltage window, ranging from 2.5 to 2.8 V [118]. AC/CB LA133 could achieve high voltages (2.6 V) with gravimetric capacitance, gravimetric energy density, and gravimetric power density, respectively of 88.86 Fg^{-1}, 17.42 $Wh.kg^{-1}$, and 247.92 $W.kg^{-1}$. The stability of the electrochemical performance of AC/CB LA133 was measured using charge–discharge at a current density of 1 Ag^{-1} for 1000 cycles (Fig. 8**d**) and 100 cycles to compare between the binder performance (Fig. 8**e**). The results demonstrated that the AC/CB LA133 cell had a cycle life of up to 87.23% after 1000 cycles. This clearly demonstrates the excellent performance of AC/CB LA133 as a supercapacitor.

To clarify the energy storage capabilities of Ni/Si and AC/CB LA133 as supercapattery electrodes, GCD analysis was performed.

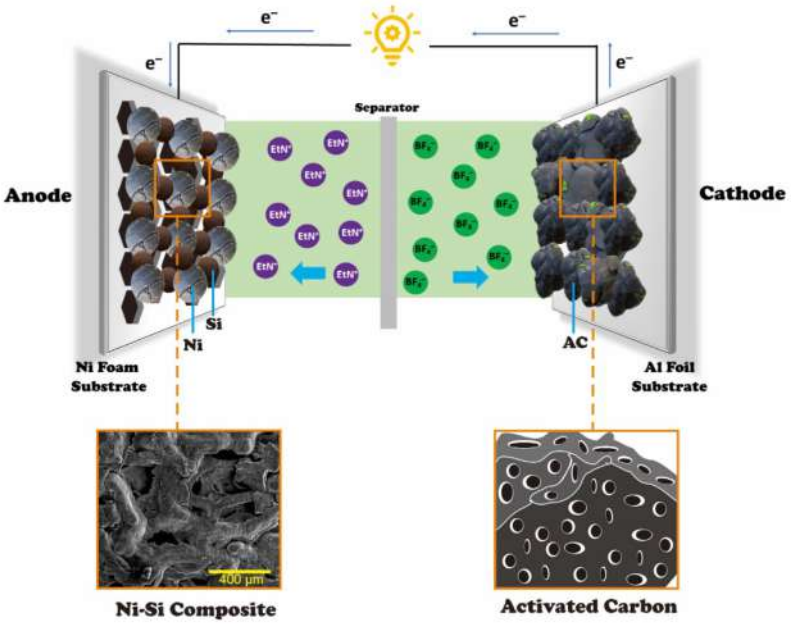

Fig. 9. Schematic illustration of electrochemical mechanism in supercapattery devices by combining two different storage processes based on activated carbon cathode and Ni/Si composite as anode.

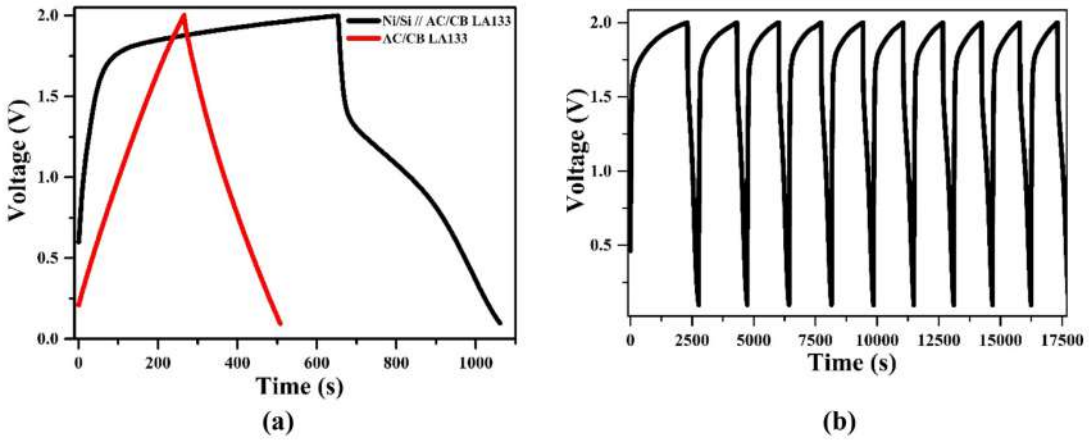

Fig. 10. Charge discharge curve of (a) AC/CB LA133 compared to Ni/Si // AC/CB LA133 and (b) stability of supercapattery for 100 cycles.

Only faradaic electroactive structures have been discovered and studied for pseudocapacitive applications; however, in recent years, most electroactive materials have been examined to reveal battery-type nonlinear characteristics during GCD analysis in organic electrolytes. As shown in Fig. 10**a, a** GCD analysis was performed at an applied potential of 2 V with current densities of 0.1 Ag^{-1} for both electrodes. The shapes of the two curves are distinctly different. Owing to the presence of Ni/Si, the curve began to resemble the characteristics of the battery. At the end of the curve, the formation of a double layer at the interface of the electrode and electrolyte causes the GCD curves to exhibit some linearity; however, the major nonlinear component in the beginning curves indicates redox reactions in the process, incorporating the two storage processes, as shown in Fig. 9 [119]. The GCD of Ni/Si // AC/CB LA133 then primarily exhibits battery-type behavior and a small amount of EDLC from activated carbon, which is typically an inverted sharp "V" type plot [120]. Additionally, it should be noted that the discharge time of the Ni/Si // AC/CB LA133 electrode is considerably longer than that of the intrinsic AC/CB LA133 electrode, indicating a higher capacity of the supercapattery electrode. The Ni/Si // AC/CB LA133 supercapattery exhibit 16.46 Fg^{-1}. These results are obtained by computing the supercapattery gravimetric capacitance without using the multiplier factor of 4 in equation 3, which will cause the value to be smaller. Even so, further research is required to maximize the performance of supercapacitors that use Ni/Si materials as the battery side and LA133 as the binder. The results of this study serve as a starting point for this kind of research. Fig. 10**b** illustrates the stability of the GCD supercapattery curve, which represents a linear curve with a minimal shape change for 100 cycles, indicating good electrochemical performance.

This good performance was also due to the LA133 binder used in the Ni/Si composite. LA133, which has historically been praised for its reliability at various voltages for anodes and cathodes, degraded in every test. This is because the cyano group and slight OH– evolution at the electrode surface interact to form a carboxylic acid group, which increases the solubility of the binder in the electrolyte [113]. Polymeric binders, such as PVDF (homopolymer) and SBR (copolymer), have weak interactions with Si. However, PVDF or SBR binders with low binding ability result in severe pulverization of Si particles, large electrode expansion, and inappropriate cycling performance of cells when faced with the incredibly large volume expansion of Si-based anodes [121].

4. Conclusions

In-depth research has been conducted to determine which binders are preferred for supporting the performance of activated carbon-based supercapacitors. After 1000 test cycles, the results indicated that LA133 was the best binder with good performance stability. This is inextricably linked to the function of the –CN group, which tends to make the binders and electrolytes more soluble. The electrochemical performance rises to 65.85 Fg^{-1} when it is utilized as a binder for Ni/Si battery electrodes and combined with AC/CB LA133 to generate a supercapattery. This demonstrates that the LA133 binder is appropriate for supercapattery to achieve the highest electrochemical performance.

Funding

This research was supported by the research fund of the Internal Universitas Negeri Malang grant program project No. 19.5.935/UN32.20.1/LT/2022.

CRediT authorship contribution statement

Markus Diantoro: Conceptualization, Validation, Formal analysis, Resources, Data curation, Writing – original draft, Writing – review & editing, Supervision, Project administration, Funding acquisition. **Istiqomah Istiqomah:** Methodology, Formal analysis, Investigation, Resources, Data curation, Writing – original draft, Writing – review & editing, Visualization, Project administration. **Oktaviani Puji Dwi Lestari:** Formal analysis, Investigation, Resources, Data curation. **Yusril Al Fath:** Visualization. **Yudyanto Yudyanto:** Software, Validation, Supervision. **Chusnana Insjaf Yogihati:** Software, Supervision. **Munasir Munasir:** Conceptualization, Validation. **Diah Hari Kusumawati:** Methodology. **Zarina Binti Aspanut:** .

Declaration of Competing Interest

The authors declare that they have no known competing financial interests or personal relationships that could have appeared to influence the work reported in this paper.

References

[1] A.N. Abdalla, M.S. Nazir, H. Tao, S. Cao, R. Ji, M. Jiang, et al., Integration of energy storage system and renewable energy sources based on artificial intelligence: An overview, J Energy Storage 40 (2021), https://doi.org/10.1016/j.est.2021.102811 102811.

[2] M. Chen, Y. Zhang, G. Xing, S.L. Chou, Y. Tang, Electrochemical energy storage devices working in extreme conditions, Energy Environ Sci 14 (2021) 3323–3351, https://doi.org/10.1039/d1ee00271f.

[3] Z. Zhang, T. Ding, Q. Zhou, Y. Sun, M. Qu, Z. Zeng, et al., A review of technologies and applications on versatile energy storage systems, Renew Sustain Energy Rev (2021) 148, https://doi.org/10.1016/j.rser.2021.111263.

[4] T. Xu, H. Du, H. Liu, W. Liu, X. Zhang, C. Si, et al., Advanced nanocellulose-based composites for flexible functional energy storage devices, Adv Mater (2021) 33, https://doi.org/10.1002/adma.202101368.

[5] A.K. Podder, O. Chakraborty, S. Islam, N. Manoj Kumar, H.H. Alhelou, Control strategies of different hybrid energy storage systems for electric vehicles applications, IEEE Access 9 (2021) 51865–51895, https://doi.org/10.1109/ACCESS.2021.3069593.

[6] A. Bouakkaz, A.J.G. Mena, S. Haddad, M.L. Ferrari, Efficient energy scheduling considering cost reduction and energy saving in hybrid energy system with energy storage, J Energy Storage 33 (2021), https://doi.org/10.1016/j.est.2020.101887 101887.

[7] H. Çınar, I. Kandemir, Active energy management based on meta-heuristic algorithms of fuel cell/battery/supercapacitor energy storage system for aircraft, Aerospace (2021) 8, https://doi.org/10.3390/aerospace8030085.

[8] M. Bolat, C. Yavuz, M. Kaya, Investigation of dual-functionalized novel carbon supported Sn material from corn stalk for energy storage and fuel cell systems on distributed generations, J Mater Sci Mater Electron 32 (2021) 18123–18137, https://doi.org/10.1007/s10854-021-06356-w.

[9] T. Salameh, M.A. Abdelkareem, A.G. Olabi, E.T. Sayed, M. Al-Chaderchi, H. Rezk, Integrated standalone hybrid solar PV, fuel cell and diesel generator power system for battery or supercapacitor storage systems in Khorfakkan, United Arab Emirates, Int J Hydrogen Energy 46 (2021) 6014–6027, https://doi.org/10.1016/j.ijhydene.2020.08.153.

[10] W. Pinthurat, B. Hredzak, Fully decentralized control strategy for heterogeneous energy storage systems distributed in islanded DC datacentre microgrid, Energy 231 (2021), https://doi.org/10.1016/j.energy.2021.120914 120914.

[11] O. Gerard, A. Numan, S. Krishnan, M. Khalid, R. Subramaniam, R. Kasi, A review on the recent advances in binder-free electrodes for electrochemical energy storage application, J Energy Storage 50 (2022), https://doi.org/10.1016/j.est.2022.104283 104283.

[12] S. Rajeevan, S. John, S.C. George, The effect of poly(vinylidene fluoride) binder on the electrochemical performance of graphitic electrodes, J Energy Storage 39 (2021), https://doi.org/10.1016/j.est.2021.102654 102654.

[13] G. Pan, Z.-B. Ding, N. Fu, G. Zhang, W. Zu, Y. Zhan, et al., Electron transfer accelerated polymer-TiO2 coatings for enhanced photocatalytic activity in photocathodic protection, Appl Surf Sci 599 (2022), https://doi.org/10.1016/j.apsusc.2022.153984 153984.

[14] X. Qiao, C. Wang, J. Zang, B. Guo, Y. Zheng, R. Zhang, et al., Conductive inks composed of multicomponent carbon nanomaterials and hydrophilic polymer binders for high-energy-density lithium-sulfur batteries, Energy Storage Mater 49 (2022) 236–245, https://doi.org/10.1016/j.ensm.2022.04.022.

[15] A.M. Pillai, P.S. Salini, B. John, M.T. Devassy, Aqueous binders for cathodes: A lodestar for greener lithium ion cells, Energy & Fuels 36 (2022) 5063–5087, https://doi.org/10.1021/acs.energyfuels.2c00346.

[16] C.Y. Huang, C.W. Chiu, Facile fabrication of a stretchable and flexible nanofiber carbon film-sensing electrode by electrospinning and its application in smart clothing for ECG and EMG monitoring, ACS Appl Electron Mater 3 (2021) 676–686, https://doi.org/10.1021/acsaelm.0c00841.

[17] C.P. McCord, T. Ozer, C.S. Henry, Synthesis and grafting of diazonium tosylates for thermoplastic electrode immunosensors, Anal Methods 13 (2021) 5056–5064, https://doi.org/10.1039/D1AY00965F.

[18] L. Zhang, W.-B. Zhang, S.-S. Chai, X.-W. Han, Q. Zhang, X. Bao, et al., Review—Clay Mineral Materials for Electrochemical Capacitance Application, J Electrochem Soc 168 (2021) 70558, https://doi.org/10.1149/1945-7111/ac163b.

[19] M.M. Baig, E. Pervaiz, M. Azad, Z. Jahan, M.B. Khan Niazi, S.M. Baig, NiFe2O4/SiO2 nanostructures as a potential electrode material for high rated supercapacitors, Ceram Int 47 (2021) 12557–12566, https://doi.org/10.1016/j.ceramint.2021.01.113.

[20] S. Majid, A.S.G. Ali, W.Q. Cao, R. Reza, Q. Ge, Biomass-derived porous carbons as supercapacitor electrodes-A review, Xinxing Tan Cailiao/New Carbon Mater 36 (2021) 546–572, https://doi.org/10.1016/S1872-5805(21)60038-0.

[21] S. Yan, J. Lin, P. Liu, Z. Zhao, J. Lian, W. Chang, et al., Preparation of nitrogen-doped porous carbons for high-performance supercapacitor using biomass of waste lotus stems, RSC Adv 8 (2018) 6806–6813, https://doi.org/10.1039/c7ra13013a.

[22] X. Luo, Y. Chen, Y. Mo, A review of charge storage in porous carbon-based supercapacitors, New Carbon Mater 36 (2021) 49–68, https://doi.org/10.1016/S1872-5805(21)60004-5.

[23] C.K. Roy, S.S. Shah, A.H. Reaz, S. Sultana, A.N. Chowdhury, S.H. Firoz, et al., Preparation of hierarchical porous activated carbon from banana leaves for high-performance supercapacitor: effect of type of electrolytes on performance, Chem - An Asian J 16 (2021) 296–308, https://doi.org/10.1002/asia.202001342.

[24] A. Jain, M. Ghosh, M. Krajewski, S. Kurungot, M. Michalska, Biomass-derived activated carbon material from native European deciduous trees as an inexpensive and sustainable energy material for supercapacitor application, J Energy Storage 34 (2021), https://doi.org/10.1016/j.est.2020.102178 102178.

[25] M. Mansuer, L. Miao, D. Zhu, H. Duan, Y. Lv, L. Li, et al., Facile construction of highly redox active carbons with regular micropores and rod-like morphology towards high-energy supercapacitors, Mater Chem Front 5 (2021) 3061–3072, https://doi.org/10.1039/d0qm01101k.

[26] B. Akinwolemiwa, G.Z. Chen, Fundamental consideration for electrochemical engineering of supercapattery, J Braz Chem Soc 29 (2018) 960–972, https://doi.org/10.21577/0103-5053.20180010.

[27] Y. Zhao, H. Hao, T. Song, X. Wang, C. Li, W. Li, MnO2-graphene based composites for supercapacitors: Synthesis, performance and prospects, J Alloys Compd (2022) 914, https://doi.org/10.1016/j.jallcom.2022.165343.

[28] P. Sharma, V. Kumar, Current technology of supercapacitors: a review, J Electron Mater 49 (2020) 3520–3532, https://doi.org/10.1007/s11664-020-07992-4.

[29] S.E.I. Suryani, N. Sholeha, T. Suprayogi, A. Taufiq, N. Mufti, M. Diantoro, Magnetocapacitance of FC-ATiO3(A = Ba, Ca, Sr) for supercapacitor electrode, AIP Conf Proc (2020) 2251, https://doi.org/10.1063/5.0015820.

[30] Z.C. De, J.Z. Guo, Z.Y. Gu, X.T. Wang, X.X. Zhao, W.H. Li, et al., Flexible quasi-solid-state sodium-ion full battery with ultralong cycle life, high energy density and high-rate capability, Nano Res 15 (2022) 925–932, https://doi.org/10.1007/s12274-021-3577-7.

[31] J. Chang, Q. Huang, Y. Gao, Z. Zheng, Pathways of developing high-energy-density flexible lithium batteries, Adv Mater (2021) 33, https://doi.org/10.1002/adma.202004419.

[32] Q. Yang, A. Chen, C. Li, G. Zou, H. Li, C. Zhi, Categorizing wearable batteries: Unidirectional and omnidirectional deformable batteries, Matter 4 (2021) 3146–3160, https://doi.org/10.1016/j.matt.2021.07.016.

[33] C.X. Zhao, J.N. Liu, J. Wang, D. Ren, J. Yu, X. Chen, et al., A ΔE = 0.63 V bifunctional oxygen electrocatalyst enables high-rate and long-cycling zinc-air batteries, Adv Mater (2021) 33, https://doi.org/10.1002/adma.202008606.

[34] S. Li, X.-Y. Shi, Z.-P. Tang, D.-X. Li, Y.-C. Zhang, Y. Xiao, et al., Simultaneous enhancement of initial Coulombic efficiency and cycling performance of silicon-based anode materials for lithium-ion batteries, Appl Surf Sci 585 (2022), https://doi.org/10.1016/j.apsusc.2022.152643 152643.

[35] M.S.E. Houache, C. Yim, On the current and future outlook of battery chemistries for electric vehicles —, Mini Review (2023).

[36] K. Xu, X. Liu, K. Guan, Y. Yu, W. Lei, S. Zhang, et al., Research progress on coating structure of silicon anode materials for lithium-ion batteries, ChemSusChem 14 (2021) 5135–5160, https://doi.org/10.1002/cssc.202101837.

[37] C. Wu, P. Kuo, J. Duh, Reviving of silicon waste with N-doped carbon core-shell structure prepared by vapor deposition polymerization of polypyrrole applied in lithium-ion battery, Surf Coat Technol 421 (2021), https://doi.org/10.1016/j.surfcoat.2021.127418 127418.

[38] H. Chen, Z. Wu, Z. Su, S. Chen, C. Yan, M. Al-mamun, A mechanically robust self-healing binder for silicon anode in lithium ion batteries, Nano Energy (2020:), https://doi.org/10.1016/j.nanoen.2020.105654 105654.

[39] Moyassari E, Streck L, Paul N, Trunk M, Neagu R, Chang C, et al. Impact of silicon content within silicon-graphite anodes on performance and Li concentration profiles of Li-ion cells using neutron depth profiling impact of silicon content within silicon-graphite anodes on performance and Li concentration profiles of 2021. 10.1149/1945-7111/abe1db.

[40] Liu Z, Ma S, Mu X, Li R, Yin G, Zuo P. A scalable cathode chemical prelithiation strategy for advanced silicon-based lithium ion full batteries 2021. 10.1021/acsami.0c22880.

[41] Z. Cui, Q. Xie, A. Manthiram, A cobalt- and manganese-free high-nickel layered oxide cathode for long-life, safer lithium-ion batteries, Adv Energy Mater 11 (2021) 2102421, https://doi.org/10.1002/aenm.202102421.

[42] D. Zhou, X. Guo, Q. Zhang, Y. Shi, H. Zhang, C. Yu, et al., Nickel-based materials for advanced rechargeable batteries, Adv Funct Mater 32 (2022) 2107928, https://doi.org/10.1002/adfm.202107928.

[43] H. Wang, W. Shi, F. Hu, Y. Wang, X. Hu, H. Li, Over-heating triggered thermal runaway behavior for lithium-ion battery with high nickel content in positive electrode, Energy 224 (2021), https://doi.org/10.1016/j.energy.2021.120072 120072.

[44] Guo Z, Zhao S, Li T, Su D, Guo S, Wang G. Recent advances in rechargeable magnesium-based batteries for high-efficiency energy storage 2020;1903591:1–17. 10.1002/aenm.201903591.

[45] Lin Z. Recent research progresses in ether- and ester-based electrolytes for sodium-ion batteries 2019:1–14. 10.1002/inf2.12023.

[46] Zhao J, Yang X, Li S, Chen N, Wang C, Zeng Y, et al. Hybrid and aqueous Li + – Ni metal batteries 2021;3:2498–508. 10.31635/ccschem.020.202000507.

[47] M. Rastgoo-deylami, M. Javanbakht, H. Omidvar, K. Hooshyari, P. Salarizadeh, M. Bagher, Nickel-doped monoclinic WO 3 as high performance anode material for rechargeable lithium ion battery, J Electroanal Chem 894 (2021), https://doi.org/10.1016/j.jelechem.2021.115383 115383.

[48] M.Z. Iqbal, M. Alzaid, U. Abbasi, S. Alam, R. Ali, A.M. Afzal, et al., Investigation of magnetron sputtered Ni@Cu/WS2 as an electrode material for potential supercapattery devices, Int J Energy Res 46 (2022) 7334–7347, https://doi.org/10.1002/er.7641.
[49] M.M. Faisal, S.R. Ali, S.S. Shah, M.W. Iqbal, S. Pushpan, M.A. Aziz, et al., Redox-active anomalous electrochemical performance of mesoporous nickel manganese sulfide nanomaterial as an anode material for supercapattery devices, Ceram Int 48 (2022) 28565–28577, https://doi.org/10.1016/j.ceramint.2022.06.170.
[50] S.G. Krishnan, A. Arunachalam, P. Jagadish, Chapter twelve - Applications of supercapattery, in: N. Arshid, M. Khalid, A.N. Grace (Eds.), Adv. Supercapacitor Supercapattery, Elsevier, 2021, pp. 311–348, https://doi.org/10.1016/B978-0-12-819897-1.00002-1.
[51] R. Bardestani, G.S. Patience, S. Kaliaguine, Experimental methods in chemical engineering: specific surface area and pore size distribution measurements—BET, BJH, and DFT, Can J Chem Eng 97 (2019) 2781–2791, https://doi.org/10.1002/cjce.23632.
[52] F. Cheng, X. Yang, S. Zhang, W. Lu, Boosting the supercapacitor performances of activated carbon with carbon nanomaterials, J Power Sources 450 (2020), https://doi.org/10.1016/j.jpowsour.2019.227678 227678.
[53] H. Yang, S. Kannappan, A.S. Pandian, J.H. Jang, Y.S. Lee, W. Lu, Graphene supercapacitor with both high power and energy density, Nanotechnology (2017) 28, https://doi.org/10.1088/1361-6528/aa8948.
[54] S. Begum, M. Ahmaruzzaman, Biogenic synthesis of SnO 2 /activated carbon nanocomposite and its application as photocatalyst in the degradation of naproxen, Appl Surf Sci 449 (2018) 780–789, https://doi.org/10.1016/j.apsusc.2018.02.069.
[55] S.N. Sari, A. Melati, Facile preparation of carbon nanofiber from banana peel waste, Mater Today Proc 13 (2019) 165–168, https://doi.org/10.1016/j.matpr.2019.03.208.
[56] Diantoro M, Istiqomah I, Fath Y Al, Mufti N, Nasikhudin N, Meevasana W, et al. Hierarchical Activated Carbon – MnO 2 Composite for Wide Potential Window Asymmetric Supercapacitor Devices in Organic Electrolyte 2022.
[57] Y.K. Lee, The effect of active material, conductive additives, and binder in a cathode composite electrode on battery performance, Energies (2019) 12, https://doi.org/10.3390/en12040658.
[58] J.E. Entwistle, G. Beaucage, S.V. Patwardhan, Mechanistic understanding of pore evolution enables high performance mesoporous silicon production for lithium-ion batteries, J Mater Chem A 8 (2020) 4938–4949, https://doi.org/10.1039/c9ta13633a.
[59] S. Liu, S.K. Tam, K.M. Ng, Dual-reductant synthesis of nickel nanoparticles for use in screen-printing conductive paste, J Nanoparticle Res (2021) 23, https://doi.org/10.1007/s11051-021-05191-8.
[60] M. Toufani, S. Kasap, A. Tufani, F. Bakan, S. Weber, E. Erdem, Synergy of nano-ZnO and 3D-graphene foam electrodes for asymmetric supercapacitor devices, Nanoscale 12 (2020) 12790–12800, https://doi.org/10.1039/d0nr02028a.
[61] H. Nishii, D. Miyamoto, Y. Umeda, H. Hamaguchi, M. Suzuki, T. Tanimoto, et al., Catalytic activity of several carbons with different structures for methane decomposition and by-produced carbons, Appl Surf Sci 473 (2019) 291–297, https://doi.org/10.1016/j.apsusc.2018.12.073.
[62] S.K. Chang, Y.J. Kim, J.Y. Lee, K.K. Choi, Thermal stability study of Ni-Si silicide films on Ni/4H-SiC contact by in-situ temperature-dependent sheet resistance measurement, Jpn J Appl Phys (2019) 58, https://doi.org/10.7567/1347-4065/ab25ba.
[63] Vatankhah AR, Malekie S, Science N, Hosseini MA. The investigation of induced structural defects in electron irradiated single- walled carbon nanotubes via Raman spectroscopy The investigation of induced structural defects in electron irradiated single-walled carbon nanotubes via Raman spectroscopy 2020.
[64] M.M. Nofal, W.O. Karim, A.S.F.M. Asnawi, J.M. Hadi, M. Fakhrul, Z. Abdul, A Polymer blend electrolyte based on CS with enhanced ion transport and electrochemical properties for electrical double layer capacitor applications, Polymers (Basel) 13 (2021) 930.
[65] S. Ren, M. Liang, W. Fan, Y. Zhang, C. Qian, Y. He, et al., Investigating the effects of SBR on the properties of gilsonite modified asphalt, Constr Build Mater 190 (2018) 1103–1116, https://doi.org/10.1016/j.conbuildmat.2018.09.190.
[66] J. Jeon, J.K. Yoo, S. Yim, K. Jeon, G.H. Lee, J.H. Yun, et al., Natural-wood-derived lignosulfonate ionomer as multifunctional binder for high-performance lithium-sulfur battery, ACS Sustain Chem Eng 7 (2019) 17580–17586, https://doi.org/10.1021/acssuschemeng.9b01924.
[67] D. Bose, S. Sridharan, H. Dhawan, P. Vijay, M. Gopinath, Biomass derived activated carbon cathode performance for sustainable power generation from microbial fuel cells, Fuel 236 (2019) 325–337, https://doi.org/10.1016/j.fuel.2018.09.002.
[68] E.S. Fathy, M.Y. Elnaggar, H.A. Raslan, Thermoplastic elastomer based on waste polyethylene/waste rubber containing activated carbon black: Impact of gamma irradiation, J Vinyl Addit Technol 25 (2019) E166–E173, https://doi.org/10.1002/vnl.21675.
[69] Y. Zhao, H. Hao, T. Song, X. Wang, C. Li, W. Li, High energy-power density Zn-ion hybrid supercapacitors with N/P co-doped graphene cathode, J Power Sources 521 (2022), https://doi.org/10.1016/j.jpowsour.2021.230941 230941.
[70] M.I. Din, M. Tariq, Z. Hussain, R. Khalid, Single step green synthesis of nickel and nickel oxide nanoparticles from Hordeum vulgare for photocatalytic degradation of methylene blue dye, Inorg Nano-Metal Chem 50 (2020) 292–297, https://doi.org/10.1080/24701556.2019.1711401.
[71] R.T. Pekarek, A. Affolter, L.L. Baranowski, J. Coyle, T. Hou, E. Sivonxay, et al., Intrinsic chemical reactivity of solid-electrolyte interphase components in silicon-lithium alloy anode batteries probed by FTIR spectroscopy, J Mater Chem A 8 (2020) 7897–7906, https://doi.org/10.1039/c9ta13535a.
[72] Z. Ali, M. Mehmood, J. Ahmad, X. Li, A. Majeed, H. Tabassum, et al., A platelet graphitic nanofiber-carbon nanotube hybrid for efficient oxygen evolution reaction, ChemCatChem 12 (2020) 360–365, https://doi.org/10.1002/cctc.201901462.
[73] T. Im, J. Pyo, Lee J. Sung, C.S. Lee, Fabrication of homogeneous nanosized nickel powders using a planetary ball mill: Applications to multilayer ceramic capacitors (MLCCs), Powder Technol 382 (2021) 118–125, https://doi.org/10.1016/j.powtec.2020.12.043.
[74] E. Eray, V. Boffa, M.K. Jørgensen, G. Magnacca, V.M. Candelario, Enhanced fabrication of silicon carbide membranes for wastewater treatment: From laboratory to industrial scale, J Memb Sci (2020) 606, https://doi.org/10.1016/j.memsci.2020.118080.
[75] W. Gao, T. Wang, J. Xu, P. Zeng, W. Zhang, Y. Yao, et al., Robust and flexible random lasers using perovskite quantum dots coated nickel foam for speckle-free laser imaging, Small 17 (2021) 1–8, https://doi.org/10.1002/smll.202103065.
[76] Ş. Sörgel, O. Kesten, A. Wengel, T. Sörgel, Nickel/sulfur composite electroplated nickel foams for the use as 3D cathode in lithium/sulfur batteries – A proof of concept, Energy Storage Mater 10 (2018) 223–232, https://doi.org/10.1016/j.ensm.2017.05.016.
[77] M. Talebi, M.M. Ahadian, S. Shahrokhian, Binder-free 3D graphene nanostructures on Ni foam substrate for application in capacitive deionization, Diam Relat Mater 120 (2021), https://doi.org/10.1016/j.diamond.2021.108612 108612.
[78] S. Krishnan, A. Arunachalam, P. Jagadish, M. Khalid, M. Nasrollahzadeh, F. Ran, et al., Pore size matters!—a critical review on the supercapacitive charge storage enhancement of biocarbonaceous materials, Crit Rev Solid State Mater Sci 48 (2022) 1–56, https://doi.org/10.1080/10408436.2022.2027225.
[79] T. Subramaniam, S. Krishnan, M.N.M. Ansari, N. Hamid, M. Khalid, Recent progress on supercapacitive performance of agrowaste fibers: a review, Crit Rev Solid State Mater Sci (2022) 1–43, https://doi.org/10.1080/10408436.2022.2052797.
[80] B. Liu, Q. Zhang, Z. Wang, L. Li, Z. Jin, C. Wang, et al., Nitrogen and sulfur-codoped porous carbon nanospheres with hierarchical micromesoporous structures and an ultralarge pore volume for high-performance supercapacitors, ACS Appl Mater Interfaces 12 (2020) 8225–8232, https://doi.org/10.1021/acsami.9b20473.
[81] S. Kim, B.S. Crandall, M.J. Lance, N. Cordonnier, J. Lauterbach, E. Sasmaz, Activity and stability of NiCe@SiO2 multi–yolk–shell nanotube catalyst for tri-reforming of methane, Appl Catal B Environ 259 (2019), https://doi.org/10.1016/j.apcatb.2019.118037 118037.
[82] H. Wang, D. Wei, H. Gang, Y. He, H. Deng, L. Hou, et al., Hierarchical porous carbon from the synergistic "Pore-on-Pore" strategy for efficient capacitive deionization, ACS Sustain Chem Eng 8 (2020) 1129–1136, https://doi.org/10.1021/acssuschemeng.9b06084.
[83] M.M. Rahman, A.Z. Shafiullah, A. Pal, M.A. Islam, I. Jahan, B.B. Saha, Study on optimum iupac adsorption isotherm models employing sensitivity of parameters for rigorous adsorption system performance evaluation, Energies (2021) 14, https://doi.org/10.3390/en14227478.
[84] F. Mikšík, T. Miyazaki, K. Thu, Adsorption isotherm modelling of water on nano-tailored mesoporous silica based on distribution function, Energies (2020) 13, https://doi.org/10.3390/en13164247.
[85] M. Sultan, T. Miyazaki, S. Koyama, Optimization of adsorption isotherm types for desiccant air-conditioning applications, Renew Energy (2018), https://doi.org/10.1016/j.renene.2018.01.045.
[86] B. Hazra, D.A. Wood, V. Vishal, A.K. Varma, D. Sakha, A.K. Singh, Porosity controls and fractal disposition of organic-rich Permian shales using low-pressure adsorption techniques, Fuel 220 (2018) 837–848, https://doi.org/10.1016/j.fuel.2018.02.023.
[87] J. Jagiello, J. Kenvin, A. Celzard, V. Fierro, Enhanced resolution of ultra micropore size determination of biochars and activated carbons by dual gas analysis using N2 and CO2 with 2D-NLDFT adsorption models, Carbon N Y 144 (2019) 206–215, https://doi.org/10.1016/j.carbon.2018.12.028.
[88] C. Schlumberger, M. Thommes, Characterization of hierarchically ordered porous materials by physisorption and mercury porosimetry—A tutorial review, Adv Mater Interfaces (2021) 8, https://doi.org/10.1002/admi.202002181.
[89] N. Liu, K. Xu, Y. Lei, Y. Xi, Y. Liu, N. Wang, et al., Germanene nanosheets: achieving superior sodium-ion storage via pseudointercalation reactions, Small Struct 2 (2021) 2100041, https://doi.org/10.1002/sstr.202100041.
[90] L.F. Zhao, Z. Hu, W.H. Lai, Y. Tao, J. Peng, Z.C. Miao, et al., Hard carbon anodes: fundamental understanding and commercial perspectives for Na-ion batteries beyond Li-Ion and K-ion counterparts, Adv Energy Mater 11 (2021) 1–28, https://doi.org/10.1002/aenm.202002704.
[91] J. Xie, P. Yang, Y. Wang, T. Qi, Y. Lei, C.M. Li, Puzzles and confusions in supercapacitor and battery: Theory and solutions, J Power Sources 401 (2018) 213–223, https://doi.org/10.1016/j.jpowsour.2018.08.090.
[92] X. Song, Q. Jiang, J. Liu, Y. Shao, Y. Feng, Enhanced electricity generation and water pressure tolerance using carbon black-based sintered filtration air-

cathodes in microbial fuel cells, Chem Eng J 369 (2019) 652–659, https://doi.org/10.1016/j.cej.2019.03.121.
[93] D. Liu, S. Li, Y. He, C. Liu, Q. Li, Y. Sui, et al., Co(OH)F@CoP/CC core-shell nanoarrays for high-performance supercapacitors, J Energy Storage 55 (2022), https://doi.org/10.1016/j.est.2022.105417 105417.
[94] M. Chen, Q. Cheng, Y. Qian, J. He, X. Dong, Alkali cation incorporated MnO2 cathode and carbon cloth anode for flexible aqueous supercapacitor with high wide-voltage and power density, Electrochim Acta 342 (2020), https://doi.org/10.1016/j.electacta.2020.136046 136046.
[95] S.J. Patil, N.R. Chodankar, Y.K. Han, D.W. Lee, Carbon alternative pseudocapacitive V2O5 nanobricks and δ-MnO2.pdf, J Power Sources (2020) 453, https://doi.org/10.1016/j.jpowsour.2020.227766.
[96] P.H. Wadekar, R.V. Khose, D.A. Pethsangave, S. Some, One-pot facile synthesis of sulfur and nitrogen co- functionalized graphene material using novel deep eutectic solvent for supercapacitor applications some 2019.pdf, Chem Sustain Chem 12 (2019) 1–11, https://doi.org/10.1002/cssc.201900953.
[97] Y. Xie, H. Du, Electrochemical capacitance of a carbon quantum dots-polypyrrole/titania nanotube hybrid, RSC Adv 5 (2015) 89689–89697, https://doi.org/10.1039/c5ra16538e.
[98] Huang Jung Jie, Y.X. Zhang, Zhang Jun Xiang, Characterization of MnO2 and AgNWs Co-doped into an activated carbon thin film electrode for supercapacitors, J Electron Mater 50 (2021) 6535–6544, https://doi.org/10.1007/s11664-021-09202-1.
[99] Y.G. Lee, G.H. An, Synergistic effects of phosphorus and boron Co-incorporated activated carbon for ultrafast zinc-ion hybrid supercapacitors, ACS Appl Mater Interfaces 12 (2020) 41342–41349, https://doi.org/10.1021/acsami.0c10512.
[100] J. Ning, M. Xia, D. Wang, X. Feng, H. Zhou, J. Zhang, et al., Superior pseudocapacitive storage of a novel Ni3Si2/NiOOH/graphene nanostructure for an all-solid-state supercapacitor, Nano-Micro Lett (2021) 13, https://doi.org/10.1007/s40820-020-00527-w.
[101] G.D. Park, S.J. Yang, J.H. Lee, Y.C. Kang, Investigation of binary metal (Ni, Co) selenite as Li-ion battery anode materials and their conversion reaction mechanism with Li ions, Small 15 (2019) 1–17, https://doi.org/10.1002/smll.201905289.
[102] Y. Anil Kumar, K. Dasha Kumar, H.J. Kim, Facile preparation of a highly efficient NiZn2O4-NiO nanoflower composite grown on Ni foam as an advanced battery-Type electrode material for high-performance electrochemical supercapacitors, Dalt Trans 49 (2020) 3622–3629, https://doi.org/10.1039/d0dt00268b.
[103] N. Duraisamy, A. Numan, K. Ramesh, K.H. Choi, S. Ramesh, S. Ramesh, Investigation on structural and electrochemical properties of binder free nanostructured nickel oxide thin film, Mater Lett 161 (2015) 694–697, https://doi.org/10.1016/j.matlet.2015.09.059.
[104] H. Sun, X. Xiao, V. Celorrio, Z. Guo, Y. Hu, C. Kirk, et al., A novel method to synthesize BiSI uniformly coated with rGO by chemical bonding and its application as a supercapacitor electrode material, J Mater Chem A 9 (2021) 15452–15461, https://doi.org/10.1039/d1ta02988f.
[105] L. Sheng, Y. Zhao, B. Hou, Z. Xiao, L. Jiang, Z. Fan, N-doped layered porous carbon electrodes with high mass loadings for high-performance supercapacitors, Xinxing Tan Cailiao/New Carbon Mater 36 (2021) 179–188, https://doi.org/10.1016/S1872-5805(21)60012-4.
[106] F. Cao, X.H. Xia, G.X. Pan, J. Chen, Y.J. Zhang, Construction of carbon nanoflakes shell on CuO nanowires core as enhanced core/shell arrays anode of lithium ion batteries, Elsevier Ltd (2015), https://doi.org/10.1016/j.electacta.2015.08.055.
[107] Su D, Xie X, Dou S, Wang G. CuO single crystal with exposed {001} facets - A highly efficient material for gas sensing and Li-ion battery applications 2014:1–9. 10.1038/srep05753.
[108] Z. Bai, Y. Zhang, Y. Zhang, C. Guo, B. Tang, A large-scale, green route to synthesize of leaf-like mesoporous CuO as high-performance anode materials for lithium ion batteries, Electrochim Acta 159 (2015) 29–34, https://doi.org/10.1016/j.electacta.2015.01.188.
[109] P. Zeng, X. Wang, M. Ye, Q. Ma, J. Li, W. Wang, et al., Excellent lithium ion storage property of porous MnCo2O4 nanorods Peiyuan, R Soc Chem (2016), https://doi.org/10.1039/C5RA26176G.
[110] Saxena P, Shukla P. A comparative analysis of the basic properties and applications of poly (vinylidene fluoride) (PVDF) and poly (methyl methacrylate) (PMMA). Springer Berlin Heidelberg; 2021. 10.1007/s00289-021-03790-y.
[111] V.K. Tiwari, A. Kumar, S. Rajkhowa, G. Tripathi, A.K. Singh, Green Solvents: Application in Organic Synthesis, Green Chem. Introd. Appl. Scope, Singapore: Springer Nature Singapore (2022) 79–112, https://doi.org/10.1007/978-981-19-2734-8_3.
[112] Y. Li, W. Lv, H. Huang, W. Yan, X. Li, P. Ning, et al., Recycling of spent lithium-ion batteries in view of green chemistry, Green Chem 23 (2021) 6139–6171, https://doi.org/10.1039/D1GC01639C.
[113] G.T. Pace, H. Wang, J.F. Whitacre, W. Wu, Comparative study of water-processable polymeric binders in LiMn 2 O 4 cathode for aqueous electrolyte batteries, Nano Sel 2 (2021) 939–947, https://doi.org/10.1002/nano.202000167.
[114] Radloff S, Scurtu R-G, Hölzle M, Wohlfahrt-Mehrens M. Applying established water-based binders to aqueous processing of applying established water-based binders to aqueous processing 2021. 10.1149/1945-7111/ac2861.
[115] S. Yao, H. Yu, M. Bi, C. Zhang, T. Zhang, X. Zhang, et al., Effect of binders on the microstructural and electrochemical performance of high-sulphur-loading electrodes in lithium-sulphur batteries, Int J Energy Res 46 (2022) 19585–19598, https://doi.org/10.1002/er.8532.
[116] L.M. Yu, Z. Luo, C.R. Gong, Y.Q. Zheng, Z.X. Zhou, H. Zhao, et al., Water-based binder with easy reuse characteristics for silicon/graphite anodes in lithium-ion batteries, Polym J 53 (2021) 923–935, https://doi.org/10.1038/s41428-021-00486-y.
[117] Y. Wei, W. Luo, Z. Zhuang, B. Dai, J. Ding, T. Li, et al., Fabrication of ternary MXene / MnO 2 / polyaniline nanostructure with good electrochemical performances, Adv Compos Hybrid Mater (2021), https://doi.org/10.1007/s42114-021-00323-z.
[118] C. Zhong, Y. Deng, W. Hu, J. Qiao, L. Zhang, J. Zhang, A review of electrolyte materials and compositions for electrochemical supercapacitors, Chem Soc Rev 44 (2015) 7484–7539, https://doi.org/10.1039/c5cs00303b.
[119] B. Akinwolemiwa, C. Peng, G.Z. Chen, Redox Electrolytes in Supercapacitors, J Electrochem Soc 162 (2015) A5054–A5059, https://doi.org/10.1149/2.0111505jes.
[120] L. Saleh Ghadimi, N. Arsalani, A.G. Tabrizi, A. Mohammadi, I. Ahadzadeh, Novel nanocomposite of MnFe2O4 and nitrogen-doped carbon from polyaniline carbonization as electrode material for symmetric ultra-stable supercapacitor, Electrochim Acta 282 (2018) 116–127, https://doi.org/10.1016/j.electacta.2018.05.160.
[121] Y.M. Zhao, F.S. Yue, S.C. Li, Y. Zhang, Z.R. Tian, Q. Xu, et al., Advances of polymer binders for silicon-based anodes in high energy density lithium-ion batteries, InfoMat 3 (2021) 460–501, https://doi.org/10.1002/inf2.12185.

A comprehensive study of binder polymer for supercapattery electrode based on activated carbon and nickel-silicon composite

ORIGINALITY REPORT

6%	6%	8%	3%
SIMILARITY INDEX	INTERNET SOURCES	PUBLICATIONS	STUDENT PAPERS

PRIMARY SOURCES

1	www.researchgate.net Internet Source	2%
2	pubmed.ncbi.nlm.nih.gov Internet Source	1%
3	umpir.ump.edu.my Internet Source	1%
4	hdl.handle.net Internet Source	1%
5	Muhammad Zahir Iqbal, Mian Muhammad Faisal, Syeda Ramsha Ali, Sidra Farid, Amir Muhammad Afzal. "Co-MOF/polyaniline-based electrode material for high performance supercapattery devices", Electrochimica Acta, 2020 Publication	1%
6	research-repository.griffith.edu.au Internet Source	1%

7 Markus Diantoro, M Istiqomah, Yusril Al Fath, M Nasikhudin, Yatimah Alias, Worawat Meevasana. " Potential of MnO - based composite and numerous morphological for enhancing supercapacitors performance ", International Journal of Applied Ceramic Technology, 2023 1%

Publication

Exclude quotes	On	Exclude matches	< 1%
Exclude bibliography	On		